AIAA JOURNAL
Vol. 36, No. 11, November 1998

Effect of Time-Varying Wake Flow Characteristics Behind Flat Plates

Jean-Michel Desse*
ONERA, Lille F-59045, France

Experimental analysis is presented of high-speed white light differential interferometry and shadow visualizations recorded at the trailing edge of flat plates that have been designed to represent the unsteady near-wake flow characteristics behind turbine blades. The effects of the boundary-layer state and thickness on the characteristics of the time-varying wake flow have been analyzed by synchronizing visualizations with unsteady pressure measurements at the trailing edge. It is shown that, when the boundary layer is turbulent, the vortex shedding frequency depends on the boundary-layer thickness, but the unsteady pressure intensity measured at the trailing edge does not. The recirculation domain is longer when the boundary layer is quasilaminar, which explains why the disturbances from the vortex street are much less perceived at the trailing edge. Finally, the analysis of interferograms and unsteady pressure indicates a strong coupling between the vortex street and the flow over the model.

Nomenclature

D = height of trailing edge
H = shape factor, δ^*/Θ
L = total length of model
L_1 = length of ogive
L_2 = length of the flat part of the model
N = vortex street frequency
P = pressure
P_0 = freestream stagnation pressure
Re = Reynolds number
Sr = Strouhal number
s = curvilinear coordinate
U_e = velocity outside the boundary layer
u = velocity
x, y = Cartesian coordinates
Δ = path difference
ΔE = optical thickness difference
Δn = refractive index difference
δ = boundary-layer thickness
δ^* = boundary-layer displacement thickness
Θ = boundary-layer momentum thickness
ρ = gas density
ρ_0 = stagnation gas density

I. Introduction

THIS work is part of a Brite–Euram project funded by the European Commission. Experimental results will be used by the partners to demonstrate the potentials of unsteady Navier–Stokes codes with large and very large eddy simulation techniques for the analysis of unsteady wake flow characteristics behind turbine blades. In turbomachinery, the vortex shedding from bladings generates acoustic resonances and structural vibrations, and it is necessary to precisely understand these phenomena to increase the lifetime and the efficiency of turbine blades. In 1967 Parker[1] showed that vortex shedding from the rotor excited acoustic resonances in a single stage compressor. Investigations of the unsteady wake flow characteristics behind turbines blades have been made by Lawaczeck and Heinemann,[2] who measured different vortex intensities in the two vortex rows. In fact, the case of vortex shedding from turbines blades is more complex than that from cylinders because the boundary-layer state at the trailing edge is not identical on the pressure and suction sides of the blade. To undertake a precise study of the unsteady near-wake flow characteristics behind turbine blades, three flat plate models have been designed with which the effects of the boundary-layer state and thickness on the characteristics of the time-varying wake flow have been tested. The models have been designed to obtain, respectively, a thick turbulent, a thin turbulent, and a quasilaminar boundary layer at the trailing edge. For all models, the boundary layers have been investigated by pitot and hot-wire probing just ahead of the separation point. The unsteady wake flows have been analyzed by high-speed visualizations based on shadow technique and on differential interferometry in white light. The unsteady pressure signals are simultaneously recorded around the trailing edge to be able to synchronize pictures and pressure variations.

Received July 16, 1997; revision received June 15, 1998; accepted for publication July 13, 1998.

*Doctor-Engineer, Department of Applied Aerodynamic, 5 Boulevard Paul Painlevé.

II. Experimental Facility

Wind Tunnel

Tests have been conducted in the Institut de Mécanique des Fluides de Lille (IMFL) two-dimensional transonic wind tunnel. The 200-mm-high and 42-mm-wide rectangular test section has slightly diverging slotted top and bottom walls. The solid side walls of the wind tunnel are equipped with interferometric quality windows, 40 mm thick and 250 mm in diameter. The stagnation conditions are very near ambiant. The freestream Mach number can be varied from 0.3 to 1. In the present tests, the Mach number measured at a reference pressure tap on the model ahead of separation has been kept constant at 0.4. Under these conditions, the unit Reynolds number is about 7×10^4 per centimeter.

Models

The models, shown in Fig. 1, are constituted of one of three ogives (L_1), a common central part (L_2), and a rear part, which is a 15-mm-thick circular trailing edge, holding most of the instrumentation. They span the width of the test section. Their trailing edge is located at the center of the wind-tunnel side-wall windows. The ogives have different lengths to get the desired boundary-layer thickness and state ahead of the base. On model A, 220 mm long, the boundary layer is expected to be thick and turbulent. On model B, 40 mm long, streamwise trip wires located on the front part of the model should yield a thin turbulent boundary layer. Finally, a quasilaminar boundary layer will be obtained with model C, 60 mm in length, the aim being to try and get the same boundary-layer thickness as on model B. The characteristics of every model are given in Table 1.

On each model, a pressure tap and a transducer have been associated on the same generatrix to obtain complete information on the pressure. The pressure taps are drilled at a diameter of 0.2 mm over a length of 3 diameters. The unsteady pressure is measured through a small hole drilled in the surface, the diameter of which has some effect on the frequency response of the transducers. This has been checked in shock tube tests of a transducer installed in a

Table 1 Characteristics of each model

Model	Ogive	L, mm	L_1, mm	L_2, mm	Width, mm	D, mm	Re, 10^{-6}	Mach
A	1	220	40	172.5	42	15	2	0.4
B	2	40	27.5	5	42	15	0.54	0.4
C	3	60	40	12.5	42	15	0.36	0.4

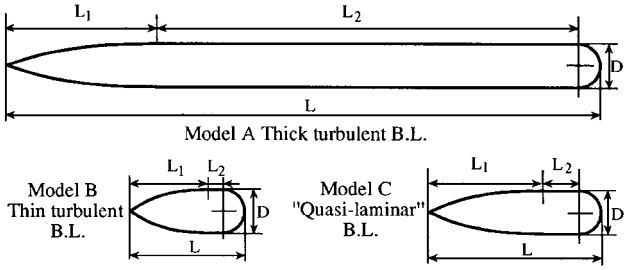

Fig. 1 Description of each model.

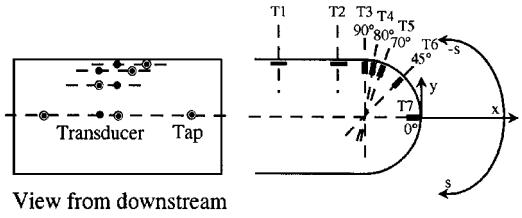

Fig. 2 Equipment at the trailing edge.

similar way. It has been observed that the hole influence decreases with increasing diameter and that for values higher than or equal to 0.8 mm it was negligible. This last value has been retained for the actual models. For the circular trailing edge of diameter 15 mm, it corresponds to an angle of only 6 deg. The equipment at the trailing edge is given in Fig. 2. Mean static pressure is measured on a mercury manometer, whereas the analog signals from the pressure transducers are digitized using several channels of LeCroy 6810 transient recorders.

A flattened pitot probe and a constant temperature hot-wire system have been used to survey the boundary layers on each model.

High-Speed Shadow System

A system called "chronoloupe" has been used to record the unsteady shadow visualizations.[3] This is a classical "Z" schlieren-shadow system (Fig. 3), symmetrical with respect to the test section, in which the light source is replaced by a battery of 24 sparks that can be triggered independently. Each spark is transformed into a parallel light beam that crosses the test section and is focused onto a receiving camera equipped with 24 lenses; 24 independent frames are thus recorded on a single 18×24 cm^2 plate. The duration of every spark is about 300 ns, and the time interval between two successive sparks is adjustable from 10^{-7} to 1 s. The first spark can be triggered with a delay varying from 10^{-7} to 1 s. The trigger signal is recorded on a channel of the transient recorder.

High-Speed White Light Interferometry

The interferometric setup (Fig. 4) usually used at IMFL is based on the differential interferometry optical setup in white light using a Wollaston prism,[4] with which a colored fringe pattern close to the Newton color scale can be observed.[5] The Wollaston prism used is of the wide-field type, which yields a uniform background color in a convergent beam. The spherical mirror is 250 mm in diameter and its radius of curvature is 2.50 m. The Wollaston prism angle is 4 deg, so that the birefringence angle is 1.25×10^{-3} rad. In the test section, an optical path difference is measured between two interfering rays shifted by 3.14 mm.

The interferograms are recorded by a CORDIN 350 high-speed rotating drum and rotating prism camera. The framing rate can reach 35,000 frames per second. The pictures are 10×8 mm^2. Tests are

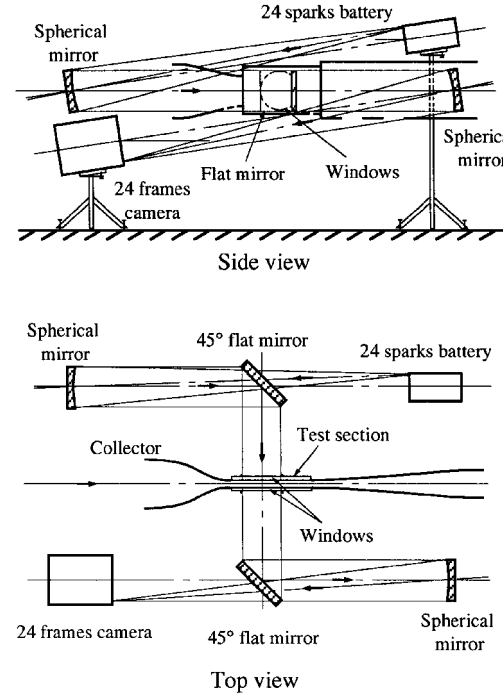

Fig. 3 IMFL setup for shadowgraph technique.

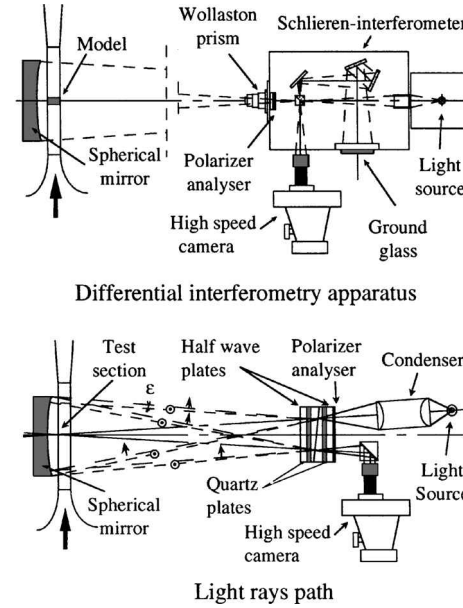

Fig. 4 High-speed differential interferometric setup.

made in complete darkness. The rotation speed of the camera is given by that of the eight-faceted internal mirror. The camera shutter stays open for time that is less than it takes for the drum to complete a revolution. At 30,000 fps, this corresponds to less than 11 ms, and the shutter is set to $\frac{1}{125}$ s. A signal corresponding to the end of the shutter opening phase is sent to the transient recorder to start signal recording and is used to trigger a flash lamp with a duration of 100 μs. The light from this lamp is conveyed through an optical fiber to the test section, enabling a precise time stamping of the pictures.

High-sensitivity (400/800 ASA) daylight reversible color films are suitable for the 150-W light source used. In the present tests, the exposure time for each interferogram is 2.5 μs, and the time interval between interferograms is 50 μs.

Processing of Interferograms

To extract quantitative information from the interferograms, IMFL has developped a technique of semiautomatic processing of the plates on a microcomputer equipped with an image processing board. The procedure, which is fully detailed in Ref. 6, yields the value of the component of the density gradient along a line perpendicular to the nonperturbed fringes. Thus, by spatial integration along this line, the density can be obtained, once a reference value is known at some place on the line.

The technique is limited, however, by the minimum path difference Δ_{min} that can be detected. Gontier[5] and Desse and Fabre[7] indicate that, under the current experimental conditions, Δ_{min} is 30×10^{-9} m, corresponding, in a two-dimensional flow 42 mm wide, to a density difference $\Delta\rho_{min} = 1.57 \times 10^{-3}$ kg/m^3 (as the light rays cross the test section twice, the actual optical thickness difference is half the path difference). As already indicated, the interfering rays are separated by 3.14 mm in the test section. Thus the smallest density gradient that can be detected is 5×10^{-4} kg/m^3/mm.

III. Results and Discussion

Steady Pressure Distributions and Boundary-Layer Characteristics

Figure 5 presents, for all three models, the static pressure distribution P/P_0 vs the curvilinear distance s/D. The tests were performed so as to ensure the same isentropic Mach number of 0.4 at the measurement location $s/D = -1.12$ (tapping P2).

The pressure distribution for model A indicates that the trailing-edge acceleration has a considerable upstream effect on the pressure, which starts to drop already at $s/D = -2.5$. The minimum pressure is reached shortly after the beginning of the trailing-edge circle at $s/D = -0.70$ at an azimuth of 80 deg. The pressure drops from about $P/P_0 = 0.912$ before the trailing edge to 0.882 at its minimum value. After the separation point the pressure rises to a plateau of $P/P_0 = 0.898$.

The limited number of pressure tappings makes it difficult to interpret the pressure distribution for the short model B. The pressure measurements upstream of the trailing edge and computational results were required to understand the experimental data [k–ϵ simulation by Meinke, Rheinisch-Westfälische Technische Hochschule Aachen (RWTH)]. The flat part of the model is too short to establish a region of constant static pressure. The pressure distribution around the trailing edge is similar to that of model A with a minimum pressure of $P/P_0 = 0.880$, compared with $P/P_0 = 0.882$, of model A, but the base pressure at the trailing-edge center is higher: $P/P_0 = 0.904$ instead of 0.898.

As regards model C, the minimum pressure is lowest of all models ($P/P_0 = 0.877$), but as the pressure rises from this minimum to 0.905, the base pressure plateau is the highest.

Boundary-Layer Characteristics

Figure 6 shows the experimental values of the velocity profiles measured with both the pitot and hot-wire probes at $x/D = -0.83$, location of transducer T2 and tap P2. The boundary-layer profiles calculated by Quemard and Archambaud[8] have been superimposed on the experimental values. The finite difference boundary-layer code uses the experimental pressure distribution and also requires an initial value for the momentum thickness, which has been adjusted so that the computed thickness at the location of the pitot surveys matches the experimental values. This, however, could not be achieved in the case of a quasilaminar boundary layer.

For model A, there exists a good agreement between the computed velocity profile for a turbulent boundary layer and the experimental data, indicating that the boundary layer is actually turbulent. For model B, the experimental data and the velocity profile are close, but the turbulent boundary layer perhaps is not quite established. For model C, the number of points within the boundary layer is probably insufficient to allow the evaluation of the shape factor H with a sufficient degree of confidence, and the comparison seems to show that the boundary layer is already transitional. Table 2 provides the different boundary-layer characteristics for each model compared with the results given by the calculation. As can be seen, on models B and C, the boundary layers have roughly the same thickness.

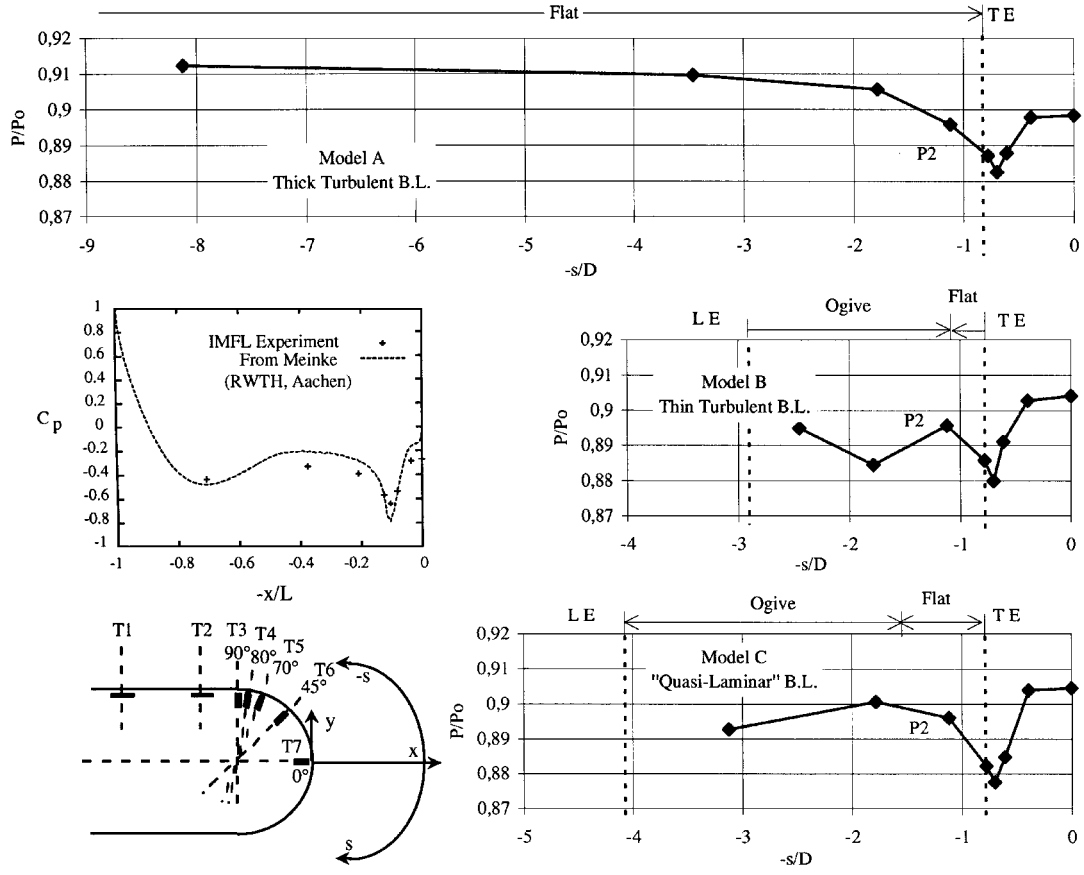

Fig. 5 Static pressure distribution on models.

Table 2 Boundary-layer characteristics for each model, $x/D = -0.83$

	Model A, thick turbulent boundary layer		Model B, thin turbulent boundary layer		Model C, quasilaminar boundary layer	
Probe	Pitot	Hot wire	Pitot	Hot wire	Pitot	Hot wire
δ/D	0.198	0.201	0.065	0.071	0.080	0.078
δ^*/D	0.0335	0.0369	0.0117	0.0118	0.0208	0.0204
Θ/D	0.0220	0.0234	0.0077	0.0071	0.0105	0.0105
H	1.52	1.57	1.52	1.67	1.99	1.95

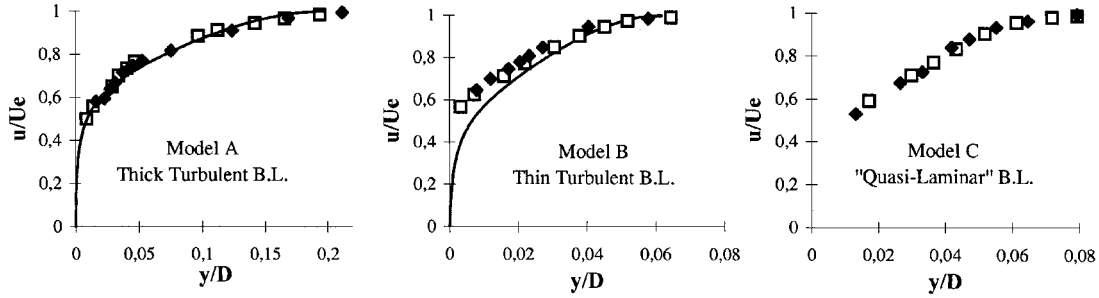

Fig. 6 Boundary-layer probings: □, pitot; ♦, hot wire; ——, Ref. 7; and $x/D = -0,83$ ($s/D = 1,120$) pressure tapping P2.

Influence of the Velocity Fluctuations on the Model

The boundary layer has been investigated at several abscissas to determine the velocity fluctuations caused by vortex shedding. This effect can be shown by progressively moving the hot wire upstream. The data are analyzed by a fast Fourier transform technique. Four probing abscissas x/D have been investigated (-0.83, -1, -1.77, and -1.33) at a constant distance of 1.1 mm from the model wall. The signals are digitized on the transient recorder. The sampling frequency is fixed at 20 kHz and the sample length at about 32,000 points. The frequency values given in Table 3 are compared with the results given by the unsteady pressure transducers at the trailing edge. The spectral analysis shows that on model A the vortex street is not perceived any more at the abscissa $x/D = -1.33$. On the other hand, there remains a weak intensity at this abscissa for model B. The probe displacement mechanism did not allow us to investigate anymore upstream. For model C the vortex street is not seen even at the abscissa $x/D = -0.83$. When the boundary layer is turbulent (either thin or thick), the disturbances induced by the vortex street are perceived up to $x/D = -1.17$ and even -1.33 for model B. This effect is not found with a quasilaminar boundary layer.

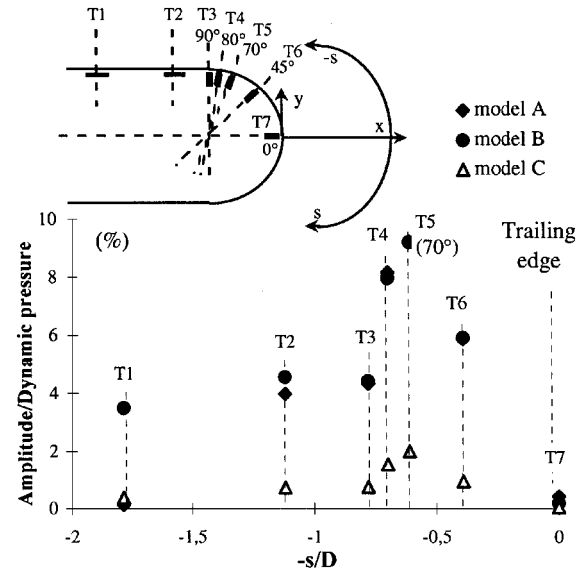

Fig. 7 Evolution of the pressure fluctuation on models.

Frequency Spectrum and Phase-Locked Average Surface Pressure Fluctuations

The pressure transducer signals were sampled at 20 and 200 kHz, and all tests have been duplicated. The length of the recording is 32,768 samples per channel, and the signals are processed using a fast Fourier transform computed using a number of points optimized so as to reduce the window effect. The amplitude of the pressure fluctuation is referenced to the dynamic pressure and is expressed in percentage. The frequencies given in Table 3 are very close to those obtained from the hot-wire probe signal. Figure 7 presents the pressure fluctuation amplitude vs the distance from the trailing edge. In all of the configurations, the largest amplitude is given by transducer T5 (azimuth 70 deg), which is easily explained by the proximity of the boundary-layer separation point. The intensities found on the turbulent boundary layer models A and B are basically identical at 8%. With the quasilaminar boundary-layer model C, the fluctuating pressure intensities are much weaker, at only 2%. It is interesting to note that the locations of the minimum mean static pressure (azimuth 70 deg) and of the maximum pressure fluctuation intensity (azimuth 80 deg) do not coincide.

Pressure fluctuations are felt upstream of separation up to the location of transducer T2 on models A and B (and even to transducer T1 on model B), which is not true for model C. This is comparable to what was observed on the velocity fluctuations.

Strouhal Number

The Strouhal numbers, based on the velocity U at pressure tap P2 ($x/D = -0.83$) and on either D or $(D + 2\delta^*)$, are given in Table 3. These values of Strouhal numbers (and of shape factors) can be compared with those found by Sieverding and Heinemann[9] in their works on the influence of boundary-layer state on vortex shedding from flat plates and turbine cascades. They have measured shape factors of 2.00 (laminar case) and 1.44 (turbulent case) near a circular trailing edge at a Mach number of 0.36. The corresponding Strouhal numbers found (0.306 for the laminar boundary layer and 0.237 for the turbulent boundary layer) have been calculated using the trailing-edge thickness increased by the pressure side and suction side boundary-layer displacement thicknesses.

In the turbulent case, our values of H compare well with those of Sieverding and Heinemann, although it is slightly higher in the case of model A. Strouhal numbers are also in good agreement for model A. In the case of model B, however, we get a higher value (0.253 compared with 0.237), which again indicates that the boundary layer is not fully turbulent on this model.

In the laminar boundary-layer case, which should be the case with model C, Sieverding and Heinemann's and our measurements of the shape factor are identical. The Strouhal number we obtain with model C (0.263) is smaller than that measured by Sieverding

Table 3 Strouhal numbers for all models

Parameter	Model A	Model B	Model C
N hot wire, Hz	2002	2262	2324
N Kulite, Hz	1947	2263	2321
D, mm	15	15	15
$D + 2\delta^*$, mm	16.10	15.35	15.61
$Sr = f \times D/U$	0.213	0.247	0.253
$Sr = f \times (D + 2\delta^*)/U$	0.228	0.253	0.263

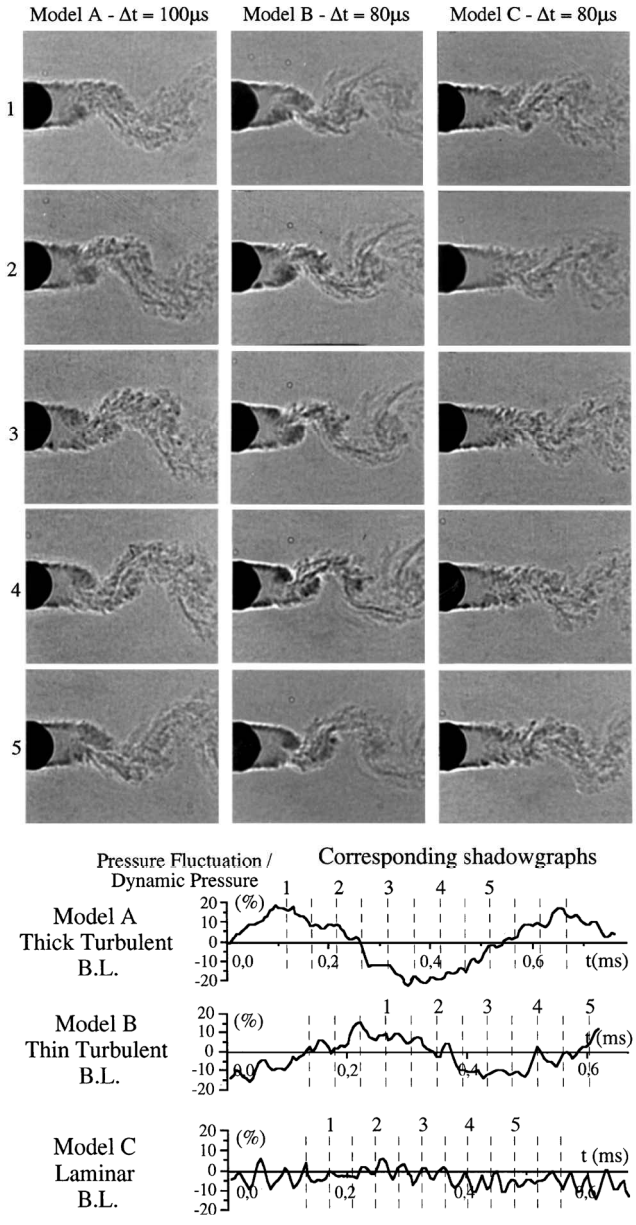

Fig. 8 High-speed shadowgraphs synchronized with unsteady pressure: transducer T5.

and Heinemann (0.306). This is another indication that the boundary layer for model C is probably transitional.

Unsteady Flow Measurements

The unsteady pressure signals recorded at a 200-kHz sampling frequency have been used to suitably synchronize the high-speed visualizations. Figure 8 shows some high-speed shadowgraphs obtained with a small displacement of the photographic plate out of the point of sharpness. The pictures are synchronized with the unsteady pressure signal from transducer T5 (close to the separation point) for the three models. A close inspection of the visualizations of Fig. 8 indicates a very strong symmetry of the vortex shedding and shows that frames 1 and 4 (model A) or 2 and 5 (model B), which show symmetrical positions of the vortices about the model symmetry axis, are basically in opposite phase. The visualizations show a large extension of the vortex street: at $x/D = 2.5$ for model A, its height is twice that of the trailing edge. The lateral space occupied by the oscillating wake is about two diameters and the freestream fluid can be seen to penetrate the wake up to the model axis. The behavior of the unsteady flow of model B is basically the same as for model A, but the visualizations of Fig. 8 show an expansion of the vortex street smaller than for model A: at $x/D = 2.5$ the height of the vortex street is only $1.5D$ and the lateral space occupied by the oscillating wake is $1.5D$. However, the penetration of the freestream into the wake is more important because it crosses the axis of symmetry of the model (frames 4 and 5).

Compared with the turbulent boundary-layer models, the trailing-edge pressure fluctuations for the quasilaminar boundary-layer case (model C) are much weaker (see transducer T5 in Fig. 8). Looking at the unsteady near wake, the amplitude of the vortex street is the smallest ($1.3D$ at $x/D = 2.5$), and it develops farther away from the trailing edge (the recirculating domain is longer). The lateral space occupied by the oscillating wake is about $1.3D$. Freestream fluid penetrating the wake is never seen to reach the axis of symmetry of the model.

Analysis of the Interferograms

A dozen interferograms covering about one period of the vortex street have been analyzed for each of the three models. Several reconstructions of interferograms and the gas density field are given for model B in Fig. 9 and for model C in Fig. 10. The results for model A are very close to those for model B and thus will not be presented here. The gas density ρ is referenced to the stagnation gas density ρ_0. In fact, because of the shifting of the two interfering rays, the interferograms can be analyzed down close to the model wall only until one of the two interfering rays is blocked by the model. In the conditions of the IMFL optical setup, the analysis is made down to 1.57 mm from the model wall and the gas density at the wall is obtained through extrapolation of the data.

First, time-averaged interferograms have been recorded using a SONY 325P video camera with the shutter adjusted at $\frac{1}{500}$ s. With this value, the visualization integrates about four or five time periods of the vortex shedding. Figures 9 and 10 show two time-averaged interferograms that are very interesting because they precisely show the mean boundaries of the recirculating domain. These visualizations confirm the fact that a difference can be found from the optical method in the lengths of the recirculating domain behind models, measured at $1.1D$ for model A and B and at about 30% more ($1.5D$) for the quasilaminar case of model C. In these interferograms optical distortion inherent to the method increases the apparent size of the mean recirculating domain by the distance between the two interfering rays (3.15 mm).

The density fields of Figs. 9 and 10 show the vortices as concentric rings, with density decreasing toward the center. These vortices undergo a formation phase where the density decreases in the vortex center, followed by a dissipation phase where the density and the size of the vortex increase. For example, in Fig. 10, the first vortex that is emitted from the lower side is in a formation phase from sketches 2–5, as indicated by a decrease of the density at the vortex center.

As previously explained, the pressure fluctuations recorded on the upper side of the model yield information on the formation and the agglomeration of the vortices shed from the upper side. Therefore, the fluctuating pressure at T5 reaches a maximum when the first large upper vortex leaves the recirculating zone (sketches 1, Figs. 9 and 10). This time indicates the start of the dissipation phase. On the contrary, the fluctuating pressure reaches a minimum when the first large lower vortex leaves (sketch 6, not shown in Fig. 10). The minimum value of the gas density obtained at the center of the vortices reaches $0.895\rho_0$ for model B and $0.886\rho_0$ for model C. At the rear mean stagnation point, on the axis of symmetry of the trailing edge, the variations of density are small around a mean value of about $0.914\rho_0$. As can be seen from Fig. 5, transducer T7 also detects very weak pressure fluctuation.

As the experiments allow one to synchronize ultrafast shadow pictures, interferograms, and unsteady pressures measured at the

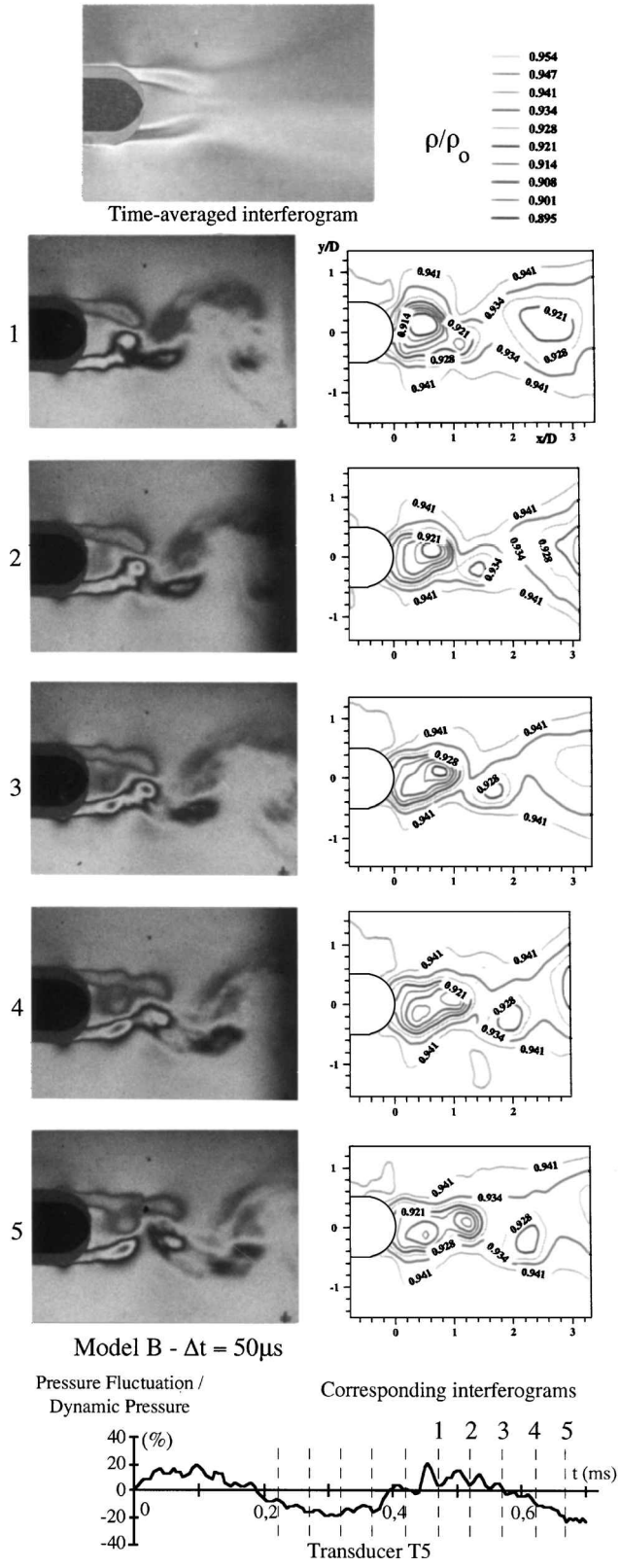

Fig. 9 High-speed interferograms synchronized with unsteady pressure: model B.

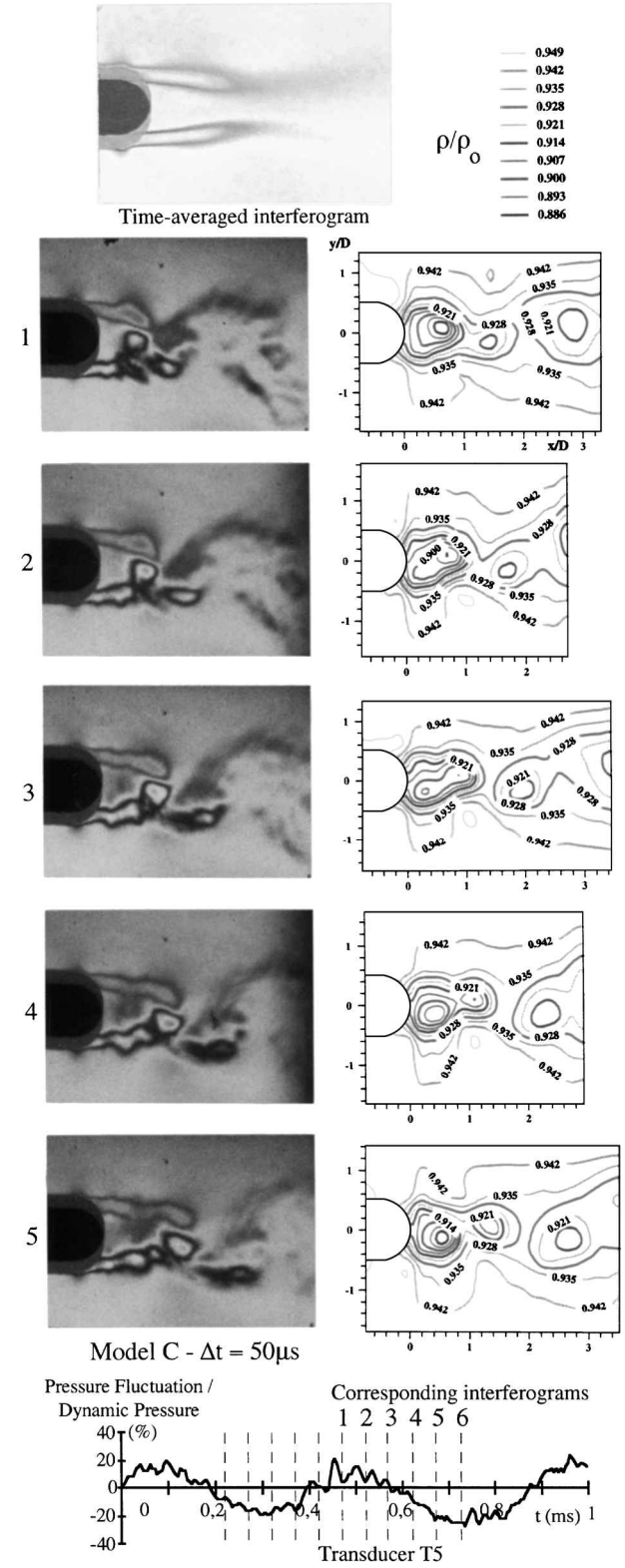

Fig. 10 High-speed shadowgraphs synchronized with unsteady pressure: model C.

trailing edge of each model, it seemed interesting to superpose a density field on a shadow picture, both obtained at the same phase of the pressure fluctuation. This comparison has been made for models B and is shown in Fig. 11, where shadowgraphs 2 and 3 correspond, respectively, to interferograms 3 and 5. In the present case shadowgraphs and interferograms have not been obtained at the same rate, and it is difficult to find exactly the corresponding frames. Nevertheless, the comparison is possible and shows a good agreement between the isodensity lines and the vortex shedding seen by the shadow technique. One can appreciate the differences in the way vortices are visualized using a shadow technique (sensitive to the second derivative of ρ) or a differential interferometry technique (sensitive to the first derivative of ρ).

A more detailed analysis for each interferogram has been made where the vortex centers have been determined. Figure 12 shows the evolution of the density at the vortex center as its abscissa from the trailing edge increases. On the three drawings it can be seen that a complete evolution of a single upper row vortex could not be found in a series of images. Consequently, it was necessary to

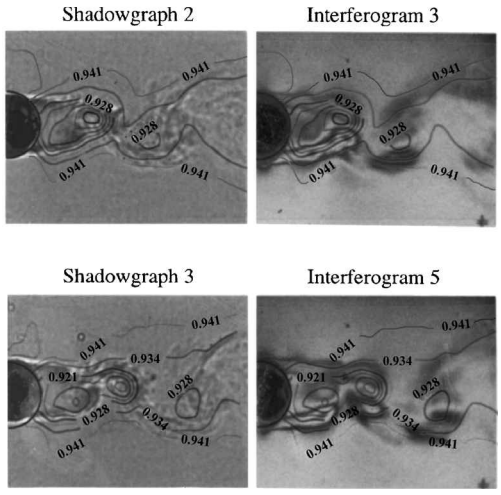

Fig. 11 Gas density field reconstruction: model B.

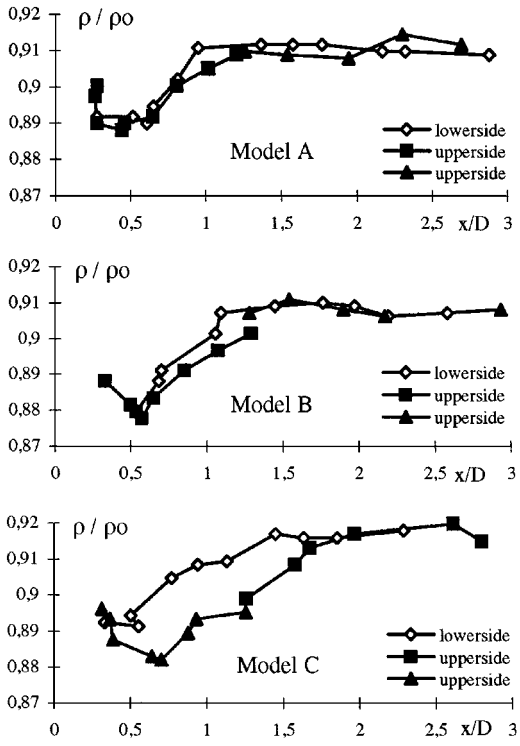

Fig. 12 *x/D* density distribution of vortex minima.

analyze two successive vortices, with a junction around $x/D = 1.25$. In all cases, density begins to decrease (formation phase) and then increases (dissipation phase). The minimum values of ρ/ρ_0 for the three models are very close to each other, between 0.877 and 0.882. In the decay phase, these values rise to 0.915 or 0.920. For model C a difference may be seen in the density of the upper row and lower row vortices: complete information on a single vortex in the lower row could not be obtained in this case either. The minimum value is 0.890 for the upper vortex and 0.882 for the lower one. The maximum value of about 0.920 is obtained in either row. For models A and B there exists a good agreement between values in the upper and lower vortices.

The accuracy of the interferograms processing can be evaluated by comparing the gas densities outside the wake at the beginning and at the end of the integration for each analyzed line. Pitot probings show that the pressures along a horizontal line are constant and equal on both sides of the wake so that the optical thickness after integration has to be equal to the initial optical thickness. After integration, a maximum difference of 0.080 μm has been found in all of the analyzed interferograms. If the yellow wavelength is taken as a reference ($\lambda = 0.560\,\mu$m), this difference in optical thickness represents about a seventh of fringe, i.e., $\Delta\rho = 8.3 \times 10^{-3}$ kg/m^3, which represents an error of 0.7% on the gas density.

Comparison with Results on a Cylinder and a Bluff Body

Comparisons can be made with results on cylinders at the same Mach number.

Rodriguez[10] has investigated the subsonic and transonic flows around a cylinder. Two transducers are implemented on a 20-mm-diam cylinder, one on a fixed part and the other one on a rotating part, to record the pressure fluctuations at several azimuths. For $M = 0.4$, the votex street frequency measured from the fluctuating pressures and the high-speed visualizations is 1350 Hz. Rodriguez shows that the amplitude of the fluctuation is very low close to the front stagnation point and increases to an almost constant value until the vicinity of the rear stagnation point is reached, where the amplitude slightly decreases. The fluctuating pressure has a maximum at azimuth 80 deg and represents about 45% of the dynamic pressure.

Rodriguez et al.[11] have also analyzed the $M = 0.4$ base flow around a blunt trailing edge by high-speed visualizations and by measurements of the fluctuating pressures. The boundary layer ahead of separation is thick and turbulent. In this case, the maximum value of the amplitude of the fluctuating pressure is reached on the model base and at 2–3% of the dynamic pressure remains very weak compared with that recorded on the cylinder. At the trailing edge the fluctuations due to the vortex street represent about 0.5% of the dynamic pressure, and they are not perceived any more upstream.

In conclusion, there exists a coupling between the vortex street and the flow over the model. When the separation points are fixed (bluff body), the amplitude of fluctuating pressures is very low. When the separation points are free to move at the trailing edge of ogive such as the models of the present work or a circular cylinder, the amplitude of the fluctuations becomes important (about 8% of the dynamic pressure for our models and 45% in the case of the circular cylinder).

IV. Conclusion

The boundary-layer momentum thicknesses obtained on models B and C are fairly close to each other. The pitot probe and the hot-wire probings are in good agreement in the determination of the boundary-layer characteristics and of the vortex shedding frequencies. When the boundary layer is turbulent (either thin or thick) the disturbances induced by the vortex street are perceived up to the central part of the model. This effect is not found with a quasilaminar boundary layer.

The unsteady pressure signals simultaneously recorded with the high-speed visualizations show that there exists a coupling between the vortex street and the flow over the models. At T5 the amplitude of the pressure fluctuation is the largest when the first large vortex leaves the recirculating domain. The vortex street effect is almost no more perceived on the transducer situated in the middle of the trailing edge.

The boundary-layer state has an influence on the length of the recirculation domain. When the boundary layer is quasilaminar (model C), the recirculation domain is longer: this explains why the disturbances from the vortex street are much less perceived at the trailing edge. The vortex street develops much farther downstream and the pressure fluctuations are much weaker (only 2 or 3% in amplitude of the dynamic pressure). When the boundary layer is turbulent (models A and B), the vortex shedding frequency depends on the boundary-layer thickness, but the unsteady pressure intensities are quite the same (about 8% of the dynamic pressure). The analysis of high-speed interferograms shows that the vortices are represented as concentric rings, with density decreasing toward the center, and that they successively pass through a formation phase where the density decreases in the vortex center and a dissipation phase where the density and the size increase.

Acknowledgments

This work has been partly funded by the European Union under Contract AER2-CT92-0048 and the Délégation Générale de l'Aviation Civile.

References

[1]Parker, R., "Resonance Effects in Wake Shedding from Compressor Blades," *Journal of Sound and Vibration*, Vol. 6, No. 3, 1967, pp. 302–309.

[2]Lawaczeck, O., and Heinemann, H.-J., "Von Karman Vortex Streets in the Wakes of Subsonic and Transonic Cascades," CP-177, AGARD, 1976, Pts. 28-1, 28-13.

[3]Dyment, A., and Gryson, P., "Etude des écoulements transsoniques turbulents par chronophotographie ultra-rapide," 13ème Colloque d'Aérodynamique Appliquée, Ecole Centrale de Lyon, Lyon, France, Nov. 1976.

[4]Desse, J. M., "Instantaneous Density Measurement in Two-Dimensional Gas Flow by High Speed Differential Interferometry," *Experiments in Fluids*, Vol. 9, No. 1–2, 1990, pp. 85–91.

[5]Gontier, G., "Contribution à l'étude de l'interférométrie différentielle à biprisme de Wollaston," Publications Scientifiques et Techniques du Ministère de l'Air, No. 338, Paris, 1957.

[6]Desse, J. M., "Recording and Processing of Interferograms by Spectral Characterization of the Interferometric Setup," *Experiments in Fluids*, Vol. 23, No. 4, 1997, pp. 265–271.

[7]Desse, J. M., and Fabre, E., "Differential Interferometry for Studying Hypersonic Flows," *Experiments in Fluids*, Vol. 20, No. 4, 1997, pp. 273–278.

[8]Quemard, C., and Archambaud, J. P., "Différences finies en couches limites bidimensionnelles avec flux de chaleur," ONERA-DERAT, Rept. 11/5005 DN, Nov. 1974.

[9]Sieverding, C. H., and Heinemann, H., "The Influence of Boundary Layer State on Vortex Shedding from Flat Plates and Turbine Cascades," *Journal of Turbomachinery*, Vol. 112, June 1990, pp. 181–187.

[10]Rodriguez, O., "The Circular Cylinder in Subsonic and Transonic Flow," *AIAA Journal*, Vol. 22, No. 12, 1984, pp. 1713–1718.

[11]Rodriguez, O., Ducruet, C., and Desse, J. M., "High Speed Visualizations Applied to Subsonic and Transonic Base Flow," *Proceedings of 4th International Symposium on Flow Visualization*, edited by C. Veret and ANRT, Hemisphere, Paris, 1986, pp. 457–462.

P. R. Bandyopadhyay
Associate Editor